RSC Advances

PAPER

View Article Online
View Journal | View Issue

Cite this: *RSC Adv.*, 2026, **16**, 17712

Enhanced visible-light photocatalytic degradation of hazardous organic dyes by the MCM-41 supported Bi_2S_3/CdS heterostructure

Amr Awad Ibrahim, *[ab] Yasmine Adel Younes,[acd] Salah Orabi,[a] Salma M. Abo Kamar,[ac] Doaa A. Kospa,[ac] M. M. Moawed,[a] S. A. El-Hakam [ac] and Awad I. Ahmed [ac]

Received 10th February 2026
Accepted 26th March 2026

DOI: 10.1039/d6ra01176d

rsc.li/rsc-advances

Water contamination by hazardous organic dyes raises major health and environmental issues, necessitating the development of effective and long-lasting treatment technologies. In this study, the Bi_2S_3/CdS (BS/CdS) heterostructure supported on mesoporous MCM-41 was fabricated *via* a facile and cost-effective hydrothermal method. The combination of CdS and Bi_2S_3 effectively tunes the band gap to the desired value, enabling the solar-driven photocatalysis. Moreover, the incorporation of MCM-41 with the Bi_2S_3/CdS composite enhances the surface area, structural stability, and charge carrier separation of the photocatalyst. Several electrochemical tests, including chronoamperometry (*I*–*t*), electrochemical impedance spectroscopy (EIS), linear sweep voltammetry (LSV), and Mott–Schottky analysis, were utilized to further validate the high capacity for charge transfer and the reduction of electron–hole recombination. Under visible light irradiation, the photodegradation of rhodamine B (RhB) dye was employed to assess the photocatalytic activity of the prepared samples. Among all samples, 10 MCM@BS/CdS exhibited the highest visible light degradation performance of 99.3%.

1. Introduction

Water scarcity and contamination pose significant global challenges for humanity.[1,2] Organic dyes discharged into water effluents from industries such as paper, plastics, textiles, cosmetics, pharmaceuticals, leather, and others are one of the main pollutants that have considerably contributed to water contamination.[3,4] Globally, around 7×10^7 tonnes of synthetic dyes are produced each year for the textile industry, with nearly 10% released into the environment as effluents during dyeing and processing.[5] The dye waste materials contain hazardous and cancer-causing substances that could seriously endanger human health. Even at very low concentrations (less than 1 ppm), these dyes are very detrimental to aquatic environments.[6] Moreover, dyes are engineered to be highly resistant to deterioration. This inherent stability means they are not biodegradable and can persist in the environment as toxic and carcinogenic compounds.[7] Therefore, the removal of organic dyes from wastewater is crucial. Various approaches have been applied for the dyes' removal from water, such as biodegradation,[8] coagulation,[9] adsorption,[10] membrane filtration,[11] and advanced oxidation processes (AOPs).[12] However, these methods are expensive, produce harmful byproducts and hazardous chemicals, and fail to address the wastewater issue. To avoid the drawbacks of these methods, photocatalytic degradation is considered a promising strategy for the removal of organic pollutants from wastewater.[4,13]

In recent years, advanced oxidation processes (AOPs) have been utilized as chemical treatment techniques, including photocatalysis. In the meantime, one of the most popular methods for producing reactive oxygen species (ROS), which can get rid of macromolecular organic pollutants, is photo-assisted AOPs.[14] Photocatalysis has emerged as a highly promising technology, offering a simple approach to harness energy from both natural sunlight and artificial indoor lighting.[4] Semiconductor-based catalysts increase the usefulness of photocatalysis for various important chemical processes, such as the photodegradation of organic pollutants and water splitting for hydrogen generation.[15] In the photodegradation of organic pollutants, these materials can harness solar energy to break down contaminants effectively, without generating secondary pollution.[16] Upon light absorption, they generate electrons (e^-) and holes (h^+), which drive the degradation of organic pollutants into harmless end products such as carbon dioxide and water. Moreover, photo-induced charge carriers facilitate the formation of highly reactive oxygen species (ROS), including

[a]*Chemistry Department, Faculty of Science, Mansoura University, Al-Mansoura 35516, Egypt. E-mail: amr_awad@mans.edu.eg*

[b]*Chemistry Department, College of Health and Medical Technology, Al-Farahidi University, Baghdad, Iraq*

[c]*Energy & Desalination Centre, Faculty of Science, Mansoura University, Egypt*

[d]*Nanoscience and Technology, Faculty of Science, GALALA University, Galala City, Suez, Egypt*

superoxide (O_2^-) and hydroxyl ($^{\bullet}OH$) radicals.[17] These ROS are the main species in the oxidation and degradation reactions of organic pollutants.[18] There are many semiconductor photocatalysts used in this approach due to their outstanding photocatalytic activity. Among these materials, metal chalcogenides are the most efficient catalysts due to the quick transfer of photo-generated charge carriers to the catalyst surface to oxidize the organic dyes.[19] Metal chalcogenide semiconductor-photocatalysts such as cadmium sulfide (CdS), bismuth sulfide (Bi_2S_3), zinc sulfide (ZnS), copper sulfide (CuS), and molybdenum sulfide (MoS_2) have recently garnered a lot of attention for their effective photocatalytic activity toward the water splitting, CO_2 reduction, and organic pollutants degradation.[20] Driven by the higher valence band (VB) states of their sp^3 orbitals, these materials exhibit elevated conduction band (CB) levels, which enables a more effective solar response compared to traditional metal oxide semiconductors.

Bismuth sulfide (Bi_2S_3) is a notable metal chalcogenide characterized by its extensive light absorption capabilities.[21] This material possesses great potential for photoelectrochemical (PEC) and photocatalytic applications owing to its narrow bandgap (~1.3 eV), high dielectric permittivity, layered structure, and highly tunable energy levels.[22] Additionally, the tubular topology and distinctive morphology of Bi_2S_3 nanostructures can extremely enhance their physical properties and charge capacity.[23] However, the widespread application of Bi_2S_3 in photocatalysis is limited by its narrow bandgap, which leads to rapid electron–hole recombination.[24] Hence, Bi_2S_3 nanoparticles can be engineered through heterojunction formation, addressing these activity limitations. The heterojunction of a carefully chosen semiconductor with the Bi_2S_3 structure can possess suitable energy levels promoting efficient charge transfer, resulting in enhanced photocatalytic activity.

Among highly effective solar-driven photocatalysts, cadmium sulfide (CdS) stands out owing to its advantageous properties.[25] Its narrow bandgap of approximately 2.42 eV allows for efficient absorption of visible light, while its significantly negative conduction band potential provides strong reducing power.[26] Together, these features result in its exceptional photo-excitation capabilities and remarkable overall catalytic performance.[27] Despite its promise, the practical application of CdS is hindered by significant limitations. Chief among these is the strong tendency of CdS nanoparticles to aggregate into larger clusters. This agglomeration is detrimental for two key reasons: it drastically reduces the available specific surface area, thereby decreasing the number of active catalytic sites. Also, it simultaneously accelerates the photogenerated e^-/h^+ pairs recombination.[28] In addition, in an aqueous solution, CdS itself is exposed to photocorrosion as it is oxidized by photo-generated holes within the photo-catalytic reaction.[29]

CdS can be incorporated with other semiconductors to boost the separation of photogenerated h^+/e^-, and this is considered one of the best methods for solving CdS problems.[30] The strategic alignment of the energy bands in a Bi_2S_3/CdS composite, where the conduction and valence bands of CdS are more negative and positive than those of Bi_2S_3, has been shown in previous reports to boost light-harvesting capabilities while significantly improving charge separation and photosensitivity. For instance, studies have successfully synthesized composites that exhibit improved photocatalytic or photochemical properties, such as Bi_2S_3@CdS@RGO,[23] MoS_2/CdS/Bi_2S_3,[31] CdS/Bi_2S_3-vS,[32] and CdS/Bi_2S_3/$BiOIO_3$.[33] Conventional photocatalysts face several challenges, including limited stability, low efficiency in visible light utilization, and insufficient capability to remove persistent organic pollutants. A variety of support materials, including activated carbon,[34] silica,[35] zeolites,[36] and alumina clays,[37] have been utilized to immobilize photocatalysts.

Among mesoporous silica materials, MCM-41 is particularly notable for its wide use and outstanding structural features, such as high surface area, uniform pore size distribution, ease of independent surface functionalization (both internal and external), a gating mechanism for pore opening, and tunable pore architecture.[38,39] These characteristics facilitate effective mass transfer, the availability of active sites, and the possibility for accurate regulation of catalytic selectivity. The Bi_2S_3/CdS photocatalytic activity can be markedly affected upon incorporation into MCM-41 support, which possesses numerous active sites and a high surface area for reactions. The acidic characteristics of MCM-41 also enhance the dye adsorption near the active sites, promoting photocatalytic degradation. Additionally, the uniformly arranged channels of MCM-41plays a key role in controlling Bi_2S_3/CdS particle size, avoiding its agglomeration. Meanwhile, MCM-41 can improve the interfacial charge transfer from the Bi_2S_3/CdS to the substrate, reducing electron–hole recombination.

In this study, the Bi_2S_3/CdS photocatalyst was incorporated into MCM-41 as a support at different loadings. To evaluate the photocatalytic activity of different photocatalysts, rhodamine B dye was employed as a model pollutant, and its degradation mechanism was further explored through quenching experiments. To assess the effectiveness of photodegradation performance, multiple factors were investigated, including the amount of the MCM support, the pH of the dye solution, and the concentration of organic pollutants. The novelty of this study comes from the controlled incorporation of Bi_2S_3/CdS into mesoporous MCM-41, where the mesoporous MCM-41 support not only enhances light absorption and charge separation but also improves stability and reusability. Moreover, the synergistic assessment of photoelectrochemical and photocatalytic properties offers deeper insight into the intrinsic performance of the composite. Accordingly, the as-prepared catalyst exhibited outstanding visible-light-driven photocatalytic activity, achieving 99.3% RhB degradation within 60 min and following pseudo-first-order kinetics with excellent stability over multiple cycles.

2. Experimental

2.1. Materials and reagents

Ammonium hydroxide solution (33%), tetraethyl orthosilicate (TEOS), bismuth nitrate ($Bi(NO_3)_3 \cdot 5H_2O$), anhydrous cadmium chloride ($CdCl_2$), thiourea (H_2NCSNH_2), ethylene glycol ($HOCH_2CH_2OH$), cetyl trimethyl ammonium bromide (CTAB),

and rhodamine B were ultra-pure. All necessary reagents were purchased from Sigma-Aldrich and used directly as supplied without any purification.

2.2. Preparation of photocatalysts

2.2.1. Preparation of mesoporous MCM-41. The pure silica MCM-41 synthesis was conducted following the foundational procedure originally reported by Beck.[40] 2.0 g CTAB is added to 100 mL of H_2O under stirring till a clear solution appears, followed by the addition of 12.5 mL of 33 wt% ammonia solution in water. An ammonia solution produces a strongly basic medium, typically with a pH ranging from 13.0 to 14.0. After vigorous stirring for approximately 30 minutes, 10.0 mL of TEOS is added to the clear solution, forming a thick white mixture that typically requires manual stirring to achieve uniform gel homogeneity. The product was filtered, washed with distilled water to ensure the removal of excess CTAB and ammonia, and dried in air at 120 °C, giving a fluffy and white powder. The mole composition of the gel mixture was CTAB : TEOS : ammonia : H_2O = 0.22 : 1.04 : 1.39 : 44.4, respectively.

A high surface area mesoporous material is obtained by removing the surfactant template through high-temperature calcination, leaving behind a silica framework with hexagonally ordered pores. The samples were placed in a ceramic vessel and heated in a muffle furnace at 550 °C, with a ramp rate of 5 °C min^{-1} for 6 hours. This temperature can eliminate the organic template while preserving the structural integrity of the mesoporous silica. The resulting material, referred to as MCM-41, is stored in a desiccator to prevent water adsorption on its surface.

2.2.2. Preparation of Bi_2S_3/CdS (BS/CdS) heterostructure. The heterostructure BS/CdS was synthesized *via* the hydrothermal method.[41] The precursor ratios were selected based on prior optimization experiments evaluating heterostructure formation and performance. In the preparation of BS/CdS, 2.96 mmol of thiourea, 0.24 mmol of anhydrous $CdCl_2$, and 1.8 mmol of $Bi(NO_3)_3 \cdot 5H_2O$ were incorporated into 45 mL of ethylene glycol, followed by sonication for a duration of 10 minutes. Then, the solution was stirred for 60 minutes at room temperature and transferred into a 50 mL Teflon-lined stainless-steel autoclave. The mixture was then sealed and maintained at 180 °C for 4 h. The resulting black solid was centrifuged, repeatedly washed with ethanol and distilled water, and dried at 100 °C for 3 h.

2.2.3. Preparation of MCM@Bi_2S_3/CdS heterostructure. The as-prepared mesoporous MCM-41 was impregnated with a solution of thiourea, anhydrous $CdCl_2$, $Bi(NO_3)_3 \cdot 5H_2O$, and 45 mL of ethylene glycol. The mixture was then sonicated for 10 minutes and stirred for 60 minutes at room temperature. Finally, it was transferred into a 50 mL Teflon-lined stainless-steel autoclave and subjected to hydrothermal treatment at 180 °C for 4 h. The final black solid product was centrifuged, washed with ethanol and distilled water several times, and dried at 100 °C for 3 h. Four samples of MCM@BS/CdS heterostructure were prepared with different ratios of MCM (5, 7, 10, and 15%) and labelled as 5MCM@BS/CdS, 7MCM@BS/CdS, 10MCM@BS/CdS, and 15MCM@BS/CdS.

2.3. Materials characterization

Several analytical techniques were used to characterize the as-synthesized samples. X-ray diffraction patterns (XRD) at 2θ between 4 and 70° were used to further analyse the samples using a Bruker apparatus. The morphology of the as-synthesized materials was verified using scanning electron microscopy (SEM, JEOL JSM 6510 lv), transmission electron microscopy (TEM, Joel JEM-2100), and X-ray spectroscopy (EDS). The band gap of as-synthesized heterostructure materials was obtained from the absorbance and wavelength values using UV-vis diffuse reflectance spectroscopy (ATIUNICAM-UV/VISIBLE VISION SOFTWARE V3.20). X-ray photoelectron spectroscopy (XPS) was carried out using a PREVAC EA15 system equipped with a 180° hemispherical electrostatic analyzer (HSA) and a monochromatic Al Kα X-ray source (1486.6 eV) operating at 12 kV and 25 mA. The concentrations of the organic dye rhodamine B during photocatalytic degradation were measured using a PerkinElmer Lambda 2 UV/vis spectrophotometer (Unicom 5625, USA). Electrochemical measurements were conducted using a Corrtest potentiostat and a SciSun-300 solar simulator (Class AAA, 300 W, 50 × 50 mm) as a solar light source.

2.4. Electrochemical measurements

A conventional three-electrode cell was used for all photoelectrochemical measurements, which were conducted at ambient temperature. The electrochemical cell, controlled by a Corrtest potentiostat, consisted of a platinum (Pt) wire counter electrode, an Ag/AgCl reference electrode, and a sample-coated indium tin oxide (ITO) glass as the working electrode. The conducted potentials were converted to the RHE scale in accordance with the Nernst equation as follows:

$$E(\mathrm{RHE}) = E(\mathrm{Ag/AgCl}) + E^{\circ}(\mathrm{Ag/AgCl})(0.197\ \mathrm{V}) + 0.059 \times \mathrm{pH} \quad (1)$$

In a 1 mL tube, the as-prepared catalyst was sonicated in a solution containing 450 μL of absolute ethanol and 20 μL of 5 wt% Nafion, preparing the photocatalyst ink. Subsequently, an active area (1 cm × 1 cm) of a pre-cleaned indium tin oxide (ITO) substrate was drop-cast with 10 μL of the resulting suspension and allowed to dry completely under ambient conditions. To determine the background capacitive current of the synthesized materials, the photocurrent density (*J–V* curves) and linear sweep voltammetry (LSV) were measured. A SciSun-300 solar simulator equipped with an AM1.5G filter was calibrated to an output intensity of 100 mW cm^{-2} and used as a solar light source. All electrochemical measurements were performed in 1 M Na_2SO_4 electrolyte under both dark and light-irradiated conditions. For the cyclic voltammetry (CV) measurement, the potential was scanned within a window of −0.6 to 0.6 V at a rate of 200 mV s^{-1}. For EIS analysis, the 0.1 M KOH electrolyte was first deoxygenated by purging with nitrogen (N_2) gas for 15 minutes. The measurements were then

conducted at 298 K in a 100 mL cell containing 50 mL of this solution, with the frequency swept from 10^5 to 0.1 Hz.

2.5. Photocatalytic reaction

The photocatalytic degradation was employed by taking 50 mL of RhB solution (10 mg L^{-1}) with 50 mg of catalyst. The solution was exposed to a xenon light source with 300 W Xe light. The suspension was stirred magnetically to ensure that all catalyst active sites were in contact with the dye solution and adequately exposed to light. The suspensions were filtered by centrifugation to remove the suspended particles of the catalyst. Then, RhB concentration (C_t) was determined by UV-vis spectroscopy at $\lambda = 554$ nm. The percentage degradation of dyes was calculated by the following equation:

$$\text{Degradation } (\%) = \frac{C_0 - C_t}{C_0} \times 100 \quad (2)$$

where C_t is the concentration of dye at any time, and C_0 is the initial concentration of the dye (mg L^{-1}).

3. Result and discussion

3.1. Materials characterization

The XRD of all prepared materials was further investigated to determine the average crystalline properties of as-prepared samples as shown in Fig. 1a. For BS/CdS heterostructure, the orthorhombic phase of Bi_2S_3 has five peaks with 2θ values of 24.9, 28.6, 31.8, 46.7, and 52.6° corresponded with the crystal planes of (130), (211), (221), (431), and (351).[42] No obvious diffraction peak for CdS can be observed in the BS/CdS heterostructure because of the low content of CdS below the XRD detection limit, or CdS may be highly dispersed in BS/CdS; weak peaks are attributed to CdS hexagonal phase at 43.7 and 51.8°. The weak diffraction peak of CdS can be attributed to the limited amount of CdS in the heterostructure.[43] The crystal size of the BS/CdS heterostructure is 13.6 nm. For the BS/CdS heterostructure doped with MCM-41, diffraction peaks of MCM-41 cannot be observed as they appear only on low-angle X-ray diffraction patterns at 2θ values of 2.3, 4.0, and 4.8°.[44]

UV-DRS analysis was used to determine the bandgap energies of the as-synthesized nanomaterials. From the graph between the absorption coefficient *vs.* photon energy, the band gap value and its type can be determined. The band gap energy (E_g) of nanomaterials was determined by Tauc's equation.[45]

$$\alpha h\nu = A\left(h\nu - E_g\right)^{\frac{n}{2}} \quad (3)$$

where α is the absorption coefficient (a function of light frequency), ν is the incident light frequency, h is Planck's constant, and A is an energy-independent parameter. For indirect transitions of BS/CdS and 5MCM@BS/CdS, the value for n is determined to be 4. Therefore, E_g can be determined by plotting $h\nu$ *vs.* $(\alpha h\nu)^2$. The E_g values for BS/CdS and 10MCM@BS/CdS were determined to be 1.81 and 1.72 eV (Fig. 1b). The integration of Bi_2S_3 with CdS results in intermediate band gaps around 1.87–2.0 eV, which are well-suited for visible-light activity.[31] The 5MCM@BS/CdS exhibited a greater optical response in the visible region than BS/CdS due to its band gap energy (1.72 eV). Thus, increased absorption in the visible region improves the photocatalytic activity of 5MCM@BS/CdS towards dye degradation.

The surface morphology of the prepared heterostructure was determined by the TEM and SEM images, which were displayed

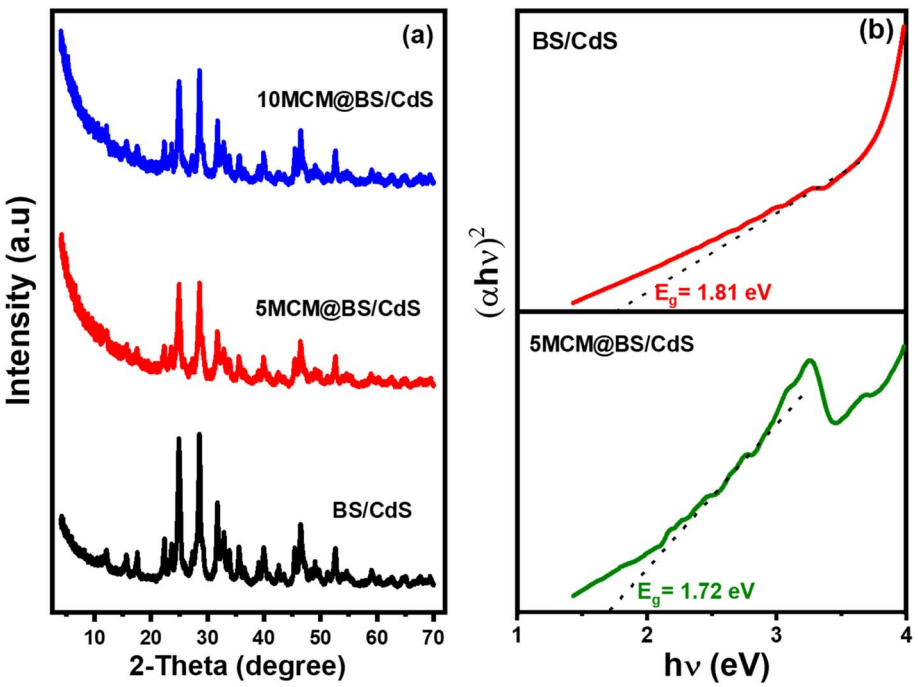

Fig. 1 (a) XRD patterns of BS/CdS, 5MCM@BS/CdS, and 10MCM@BS/CdS, and (b) band gaps of BS/CdS and 5MCM@BS/CdS.

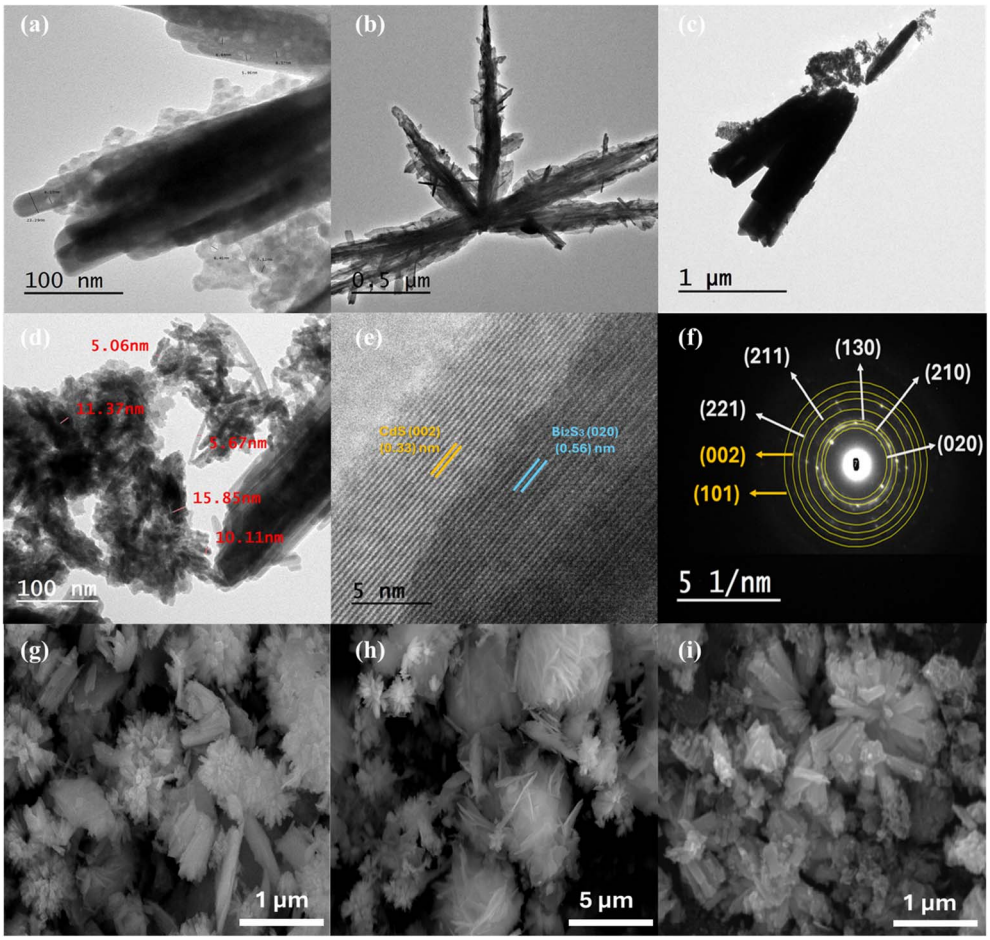

Fig. 2 TEM morphology of (a) BS/CdS, (b) 5MCM@BS/CdS, (c) 10MCM@BS/Cd with low-magnification, and (d) 10MCM@BS/Cd with high-magnification, (e) HR-TEM and (f) SAED patterns of 10MCM@BS/Cd, SEM morphology of (g) BS/CdS, (h) 5MCM@BS/CdS and (i) 10MCM@BS/CdS.

in Fig. 2. The morphology of BS/CdS heterostructure particles is revealed by transmission electron microscopy (TEM) as shown in Fig. 2a. It was observed that Bi_2S_3 has a nanorod-like shape and on its surface, small spots refer to CdS where the size of Bi_2S_3 is from 23 to 37 nm and that of CdS is from 4 to 7 nm.[46] TEM image reveals the morphological structure and uniform dispersion of the obtained BS/CdS heterostructure doped with MCM-41 samples. Fig. 2b–d show TEM images of 5MCM@BS/CdS and 10MCM@BS/CdS calcined at 550 °C, which exhibit an ordered hexagonal array of mesoporous structures.[47] The 5MCM@BS/CdS composite exhibits a more open and branched morphology, where the Bi_2S_3/CdS nanorods are partially separated and more uniformly distributed (Fig. 2b). As shown in the low-magnification TEM image (Fig. 2c), a more pronounced morphological transformation was observed with further increasing the MCM-41 content to 10 wt%. In this sample, the BS/CdS nanorods become shorter and less densely packed, indicating their incorporation within the MCM-41 matrix. Moreover, the high-magnification TEM image of 10MCM@BS/CdS (Fig. 2d) exhibits finely dispersed nanoparticles with a small size of 5–16 nm, indicating that MCM-41 effectively restricts crystal growth and enhances structural homogeneity. Moreover, the high-resolution TEM (HR-TEM) analysis was performed to demonstrate the interfacial features of 10MCM@BS/CdS composite and verify the heterojunction formation between its components. As shown in Fig. 2e, the HR-TEM image of the composite consists of two different *d*-spacing values of 0.33 and 0.56 nm, corresponding to the (020) plane of orthorhombic Bi_2S_3 and the (002) plane of hexagonal CdS, respectively. These results confirmed the coexistence of both crystalline phases and thus the successful construction of a heterojunction.[48] Moreover, the corresponding SAED image presented six concentric diffraction rings attributed to the (020), (210), (130), (211), (221) and (131) planes of Bi_2S_3 and the (002) and (101) planes of CdS, which are matched with its corresponding XRD results.

Meanwhile, the SEM image of the BS/CdS heterostructure photocatalyst exhibits densely packed flower-like microstructures composed of intergrown nanorods and platelets. These structures likely originate from the anisotropic growth of Bi_2S_3 nanorods, around which CdS particles nucleate and grow, forming a hierarchical architecture (Fig. 2g). The morphological structure of BS/CdS heterostructure doped with MCM-41, visualized by SEM, is represented in Fig. 2h and i. For 5MCM@BS/CdS, the content of MCM-41 was less than the content of the heterostructure; thus, the MCM-41 particles were dispersed on

the surface of the heterostructure base. As the content of MCM-41 increases in 10MCM@BS/CdS, the aggregation decreases, and the shape converts into nanorods. It isn't observed sharp aggregation and agglomeration for Bi_2S_3 nanorods, the 10MCM@BS/CdS composite gives more possible adsorption sites and makes the transition of electrons more rapid. Furthermore, the EDX-mapping analysis was employed to examine the elemental composition of the 10MCM@BS/CdS and to confirm the absence of any impurities (Fig. 3a–h). The presence of O, Si, S, Bi, and Cd elements in the ternary sample composition confirms the successful development of a ternary heterostructure, which indicates that the BS/CdS was decorated on the MCM.

The functional groups and chemical bonds on the surface of 10MCM@BS/CdS were identified through XPS analysis. Fig. 4a and b present the overall XPS survey and the atomic percentages of each component. Within the complete XPS spectrum, five distinct peaks are identified at 535.2, 407.7, 164.08, 160.8, and 106.08 eV, corresponding to O 1s, Cd 3d, S 2p, Bi 4f, and Si 2p, respectively. The atomic percentages determined for O 1s, Si 2p, Bi 4f, S 2p, and Cd 3d were 61.66, 24.8, 10.7, 2.18 and 0.61%, respectively. In the high-resolution spectrum of O 1s (Fig. 4c), two Gaussian peaks centred at binding energies of 533.1 and 530.7 eV were observed. These peaks are linked to O in the BiO/CdO (oxygen single bond to the bismuth and cadmium) and SiO (oxygen single bond to silicon). The Si–O bond originating from the silica framework in MCM confirms the structural presence of mesoporous silica within the complex.[49] The presence of Si–O, Bi–O, and Cd–O bonds validates the successful incorporation of Bi_2S_3 and CdS into the MCM-41 matrix. Fig. 4d illustrates that the primary peak at around 104.1 eV is associated with Si^{4+} in SiO_2 with a minor SiO_x peak (at 103.2 eV), thereby validating the existence of fully oxidized silicon atoms within the silica framework of MCM-41.[50] Furthermore, the Bi 4f spectrum (Fig. 4e) reveals two Gaussian peaks located at 164.5 and 163.1 eV, which are attributed to Bi $4f_{5/2}$. While the two peaks at 159.1 and 157.7 eV belong to Bi $4f_{7/2}$. These peaks correspond to the spin–orbit splitting of Bi $4f_{5/2}$ and Bi $4f_{7/2}$ photoelectrons, confirming the trivalent oxidation state of bismuth (Bi^{3+}) present in the Bi_2S_3 structure.[51] The small peaks centred at the region of 160.8–162.0 eV are ascribed to the S 2p present in both Bi_2S_3 and CdS components.[52] Fig. 4f shows the Cd 3d spectrum,

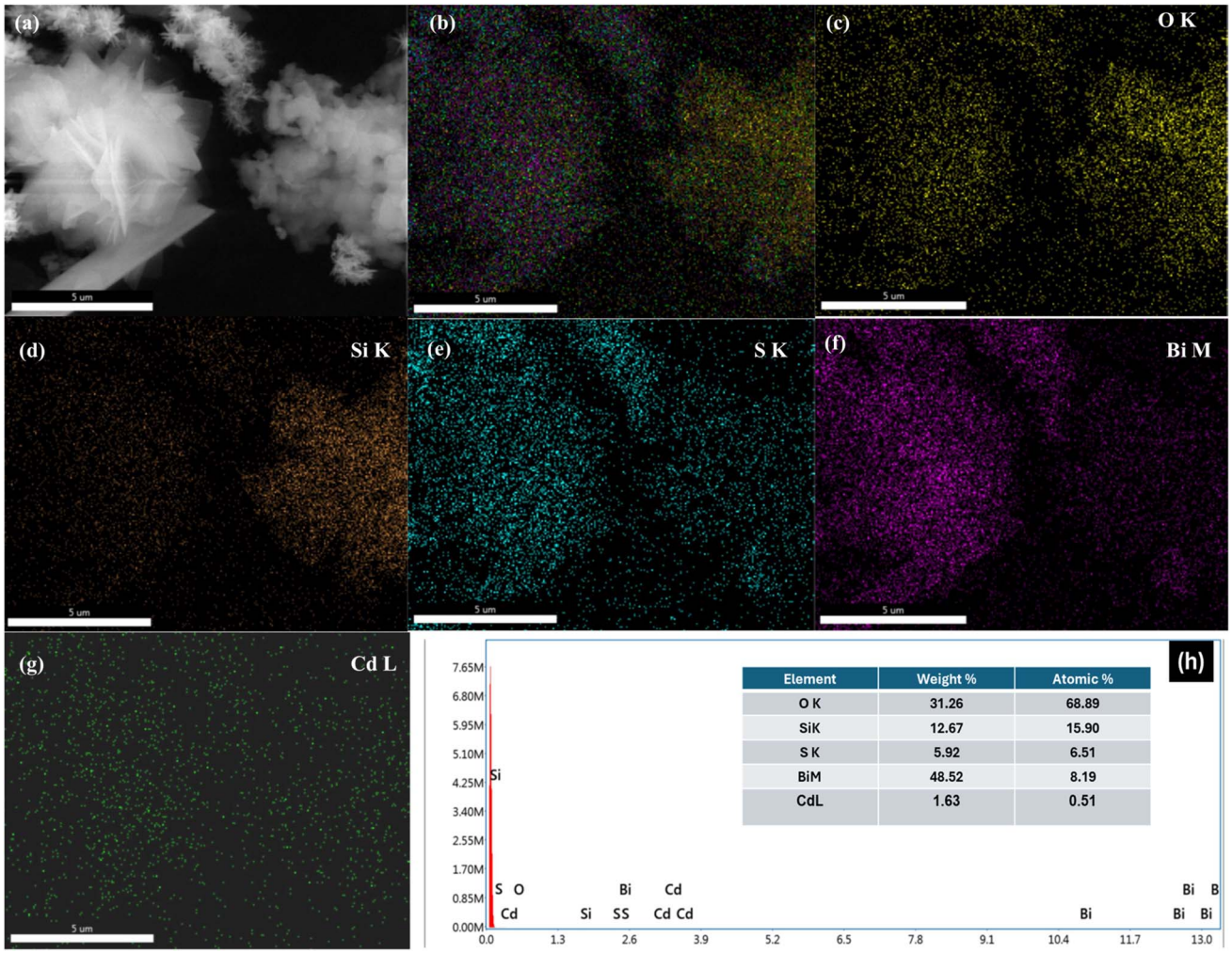

Fig. 3 (a) SEM of 10MCM@BS/CdS, EDX mapping of (b) all elements, (c) O, (d) Si, (e) S, (f) Bi, and (g) Cd, and (h) EDX pattern.

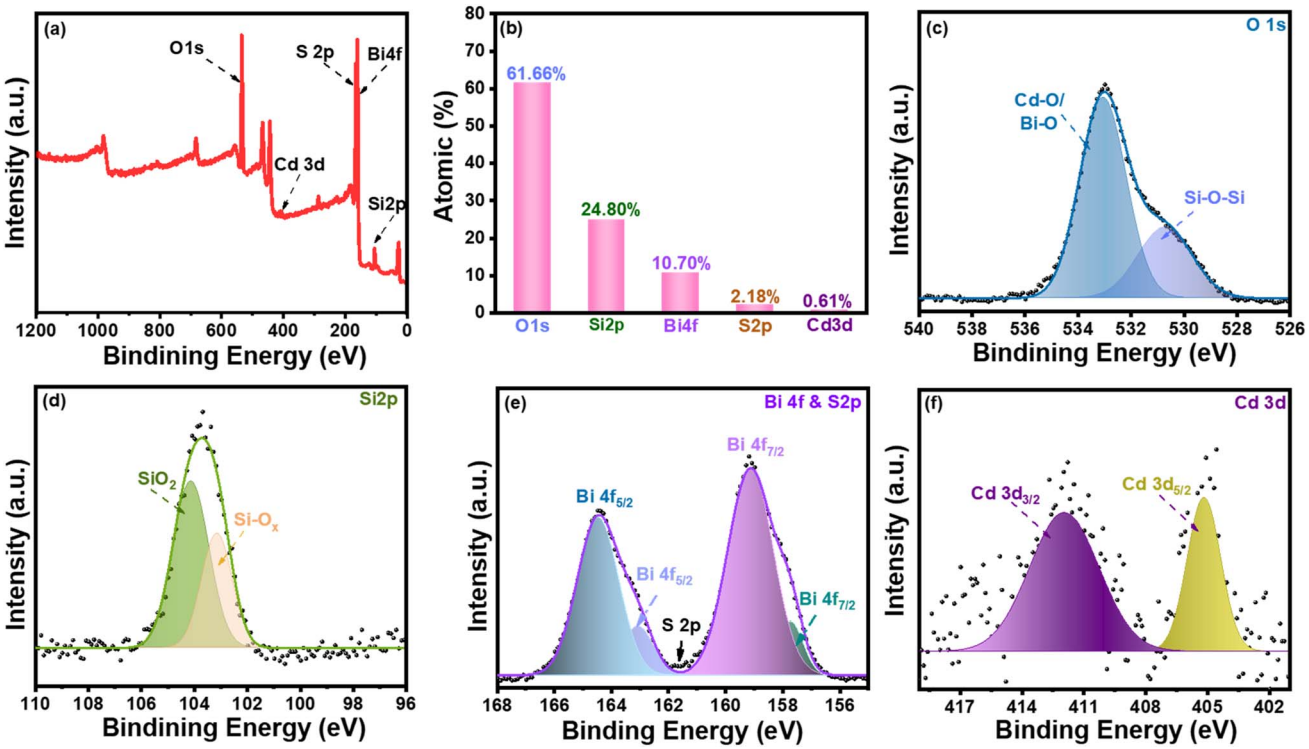

Fig. 4 XPS of 10MCM@BS/CdS, (a) total survey spectra, (b) atomic % of each component, and core-level spectra of (c) O 1s, (d) Si 2p, (e) Bi 4f, and (f) Cd 3d.

with binding energies of 411.7 eV for Cd $3d_{3/2}$ and 405.05 eV for Cd $3d_{5/2}$. The distinct peaks at these positions have been shown to correspond to CdS.[53] The XPS analysis confirms that the composition and oxidation states of the components in 10MCM@BS/CdS are consistent with the expected results.

3.2. Electrochemical study

A series of photoelectrochemical experiments was conducted to elucidate the charge carrier transport dynamics within the as-prepared photocatalysts. As depicted in Fig. 5a and b, the *I–V* curves under both dark and visible light were compared to evaluate the photoresponse of materials. Under both dark and illumination conditions, the *I–V* plots of all samples exhibit a positive correlation between current density and applied potential. At a bias of 0 V, the BS/CdS material exhibited a current density of 1 mA cm^{-2} under dark conditions. It was observed that the photocurrent density increased dramatically for all samples after light irradiation. Under the same applied bias, the recorded current densities were 0.77, 1.1, 1.3, 3.0, and 2.1 mA cm^{-2} for the BS/CdS, 5MCM@BS/CdS, 7MCM@BS/CdS, 10MCM@BS/CdS, and 15MCM@BS/CdS, respectively. Accordingly, the 10MCM@BS/CdS composite exhibits the highest photoelectrochemical activity because MCM-41 hinders the recombination of the photogenerated charge carriers. On the other hand, the chopped-light chronoamperometry (*I–t*) technique was used to evaluate the photoresponse and charge recombination of all as-prepared materials. Over eight on/off cycles of visible light (Fig. 5c), the 10MCM@BS/CdS electrode demonstrates the highest and most stable photocurrent response, achieving an approximately ~85 μA cm^{-2}. This indicates that the 10MCM@BS/CdS loading provides an ideal equilibrium among light absorption, charge carrier mobility, and surface-active sites. Conversely, excessively loading of MCM-41 in 15MCM@BS/CdS catalyst increases charge recombination or restricts light penetration, diminishing the photocurrent.

Furthermore, electrochemical impedance spectroscopy (EIS) was performed to investigate the charge transfer dynamics at the electrode–electrolyte interface. From the Nyquist plot, the semicircle diameter of the plot is related to the charge transfer resistance (R_{ct}). Accordingly, a smaller arc signifies highly efficient separation and transport of charges. Fig. 6d clearly shows the smallest semicircle arc for 10MCM@BS/CdS composite compared to other materials. These results confirm a significant reduction in charge transfer resistance, promoting faster interfacial charge transport. This enhancement facilitates charge transfer and slows down the recombination of e^-/h^+ pairs. Also, the inset in the figure shows that the resistance decreases under light irradiation compared to the dark conditions. Additionally, the flat band potentials were assessed for the synthesized photoanodes through Mott–Schottky analysis. In Fig. 5e, the potentials of FB are recorded as −0.3, −0.48, −0.51, −0.59, and −0.5 V *vs.* Ag/AgCl reference electrode (0.31, 0.13, 0.1, 0.02, and 0.11 V *vs.* RHE) at pH = 7 for BS/CdS, 5MCM@BS/CdS, 7MCM@BS/CdS, 10MCM@BS/CdS, and 10MCM@BS/CdS, respectively, derived from the interruption of the plot along the *x*-axis. The values suggest that all prepared

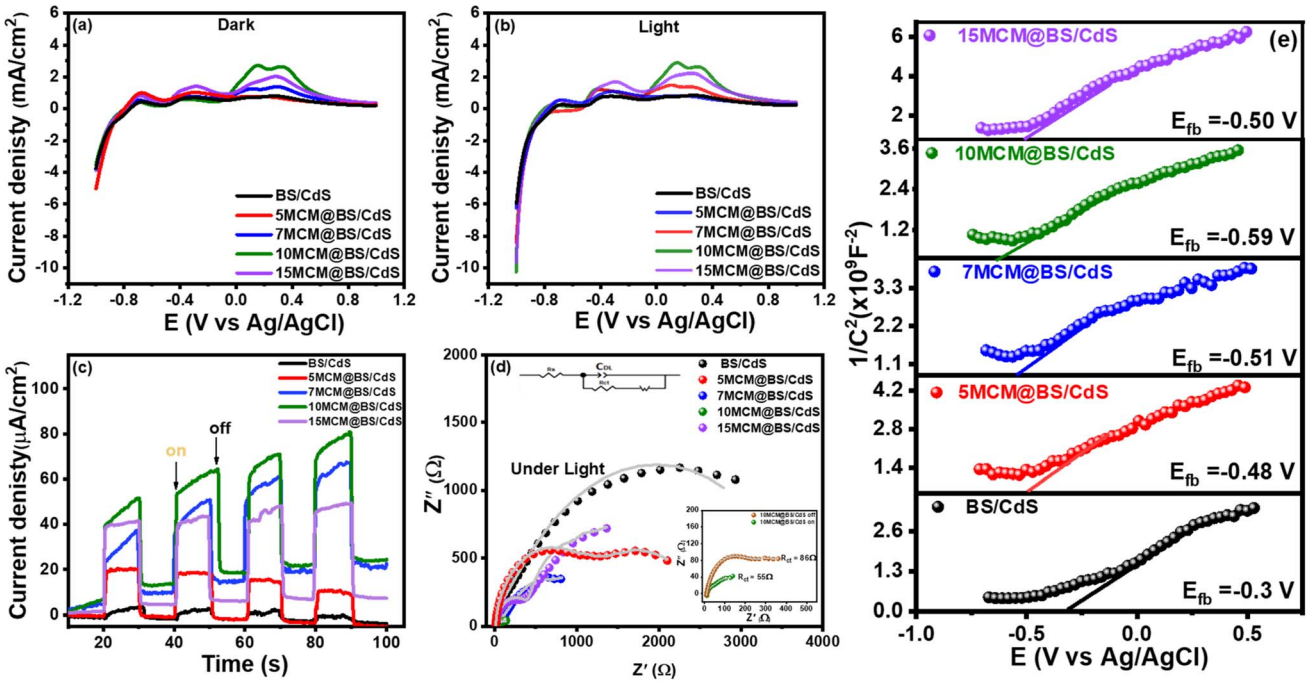

Fig. 5 LSV curve for (a) dark and (b) visible light conditions, (c) chronoamperometry technique, (d) Nyquist plot, and (e) Mott–Schottky curve.

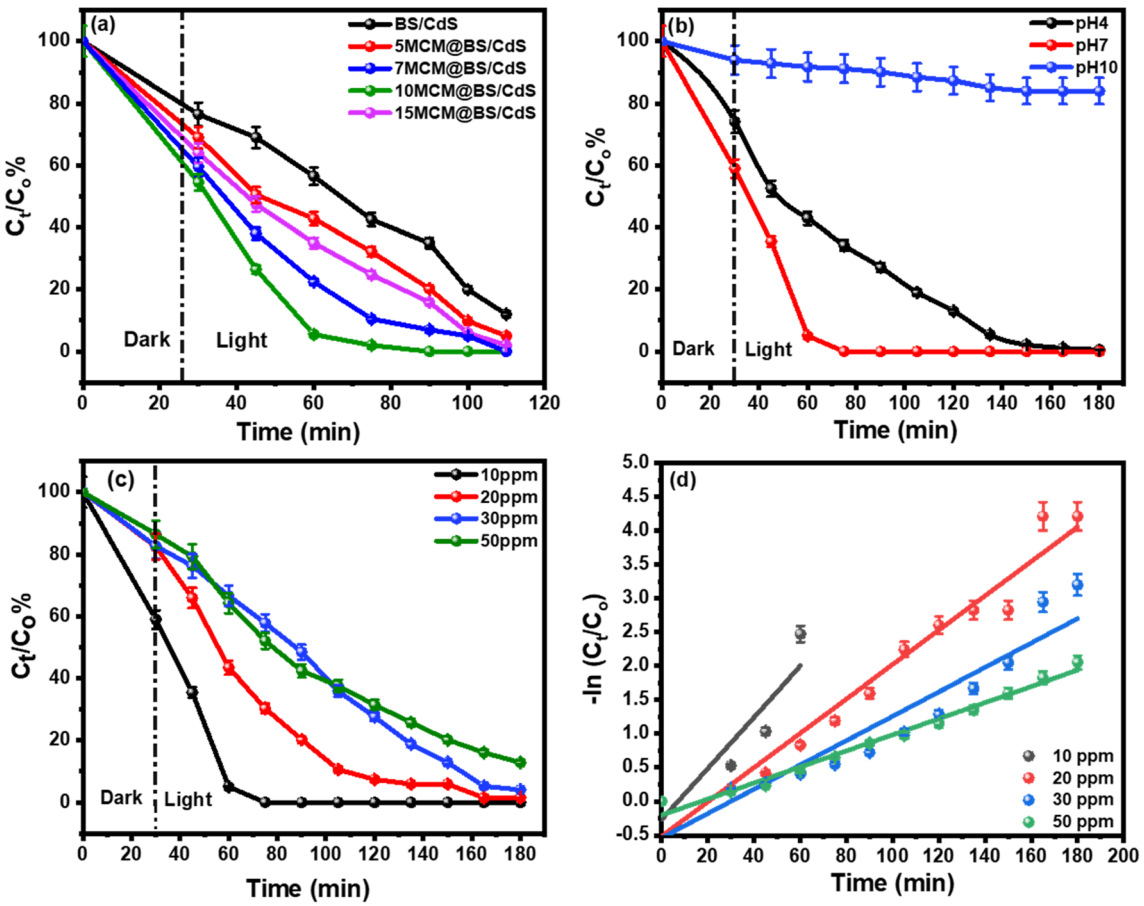

Fig. 6 %Degradation of RhB (a) effect of MCM-41 content, (b) effect of pH values, (c) effect of initial concentration of dye, and (d) first-order kinetics of the photocatalytic degradation of RhB using 10MCM@BS/CdS catalyst.

catalysts exhibit n-type semiconductor characteristics, as evidenced by the positive slopes of the curves. In n-type materials, the Fermi level is approximately close to the Fermi energy level.[4] Besides, the Mott–Schottky plot for the 10MCM@BS/CdS sample exhibits the smallest slope compared to other samples, indicating the high carrier density of this sample.[54]

3.3. The photocatalytic degradation of RhB

The organic pollutant RhB dye was chosen as a model pollutant to determine the photocatalytic activities of the as-prepared catalysts. The dye was exposed to a 400 W xenon lamp as a UV/visible light source. As illustrated in Fig. 6a, the photocatalytic activity was about 65, 79.5, 93.5, 99.3, and 85.2% within 90 min for BS/CdS, 5MCM@BS/CdS, 7MCM@BS/CdS, 10MCM@BS/CdS, and 15MCM@BS/CdS. As MCM-41 weight contents increase, photocatalytic activity increases due to the trapping effect of MCM-41 for photo-excited electrons that inhibit electron–hole recombination. However, in the case of 15MCM@BS/CdS, the photocatalytic activity diminishes, which may be due to an excessive loading of MCM that could lead to particle agglomeration or block active sites, consequently impeding effective charge mobility. The adsorption of dyes enhances visible light absorption and facilitates a fast transfer process. When Bi_2S_3 was illuminated, electrons migrated from the CB to the VB of CdS and reacted with adsorbed oxygen, giving the reactive oxygen species ($^{\bullet}O_2^-$ and $^{\bullet}OH$), which subsequently degrade the RhB dye. Overall, the obtained photocatalytic results are comparable to those reported in previous studies, as displayed in Table 1.

The pH of the dye solution mainly affected the species of RhB, charge characteristics of the photocatalyst and thus the photocatalytic system. A series of experiments with initial pH values from 2.5 to 10 was conducted to ascertain the optimal pH value for the efficacy of RhB removal utilizing the photocatalyst (Fig. 6b). Each solution was mixed with 50 mg of photocatalyst, a degradation time of 180 min, and an initial dye concentration of 10 ppm. The effect of pH on the photodegradation of RhB over 10MCM@BS/CdS was investigated under visible light irradiation. The photodegradation efficiencies were 87, 100, and 12.7% in the case of pH 4.0, 7.0, and 10.0. The photocatalysts displayed the best photocatalytic activity at pH = 7.0, but decreased in the high acidic and alkaline mediums. Excess H^+ ions in an acidic solution scavenge reactive species, inhibiting the $^{\bullet}OH$ radicals production and thus lowering the activity. Moreover, the positively charged RhB dye is repelled from the positively charged MCM@BS/CdS surface under highly acidic conditions, diminishing its adsorption and degradation rates. Conversely, the negative charge of the dye surface in the basic solution enhances the electrostatic attraction of positively charged dyes and thus promotes the adsorption rate.

On the other hand, one of the crucial factors in the organic pollutant photodegradation is its initial concentration. Thus, the photocatalytic degradation experiments were performed with different initial concentrations (10–50 ppm) of RhB solution maintained at a pH of 7 using 50 mg of 10MCM@BS/CdS. As illustrated in Fig. 6c, the efficiency of the degrading process over 10MCM@BS/CdS decreased, dropping from 99.3 to 40% as the initial RhB concentration increased from 10 to 50 ppm. The degradation rate decreases with increasing initial concentration because the lifetime of hydroxyl radicals formed is very short (only a few nanoseconds). They can only react at or near their formed location. If the dye concentration increases, the photons' entering path length will decrease, reducing the catalytic efficiency. Kinetic experiments regarding the photocatalytic degradation of RhB were conducted to substantiate the kinetic model and determine the values of the rate constant of the photocatalytic reaction. The photodegradation of RhB dye at low initial concentrations follows pseudo-first-order kinetics, consistent with the Langmuir–Hinshelwood model. The equation of relevance is as follows.

$$\ln C_0 - \ln C_t = k_{app}\, t \quad (4)$$

The expression $(C_0 - C_t)$ signifies the reduction in initial dye concentrations observed over various time intervals, while the first-order rate constant is represented by k_{app} (s^{-1}). The k_{app} values are presently derived from the slope of the graph depicting $\ln(C_0 - C_t)$ in relation to time. The linear plots corresponding to the pseudo-first-order kinetic model are shown in Fig. 6d, indicating that the RhB degradation over 10MCM@BS/CdS follows pseudo-first-order kinetics. The photocatalytic degradation kinetics of RhB over 10MCM@BS/CdS were evaluated at different initial dye concentrations (10–50 ppm). The results show that the reaction rate constant (k) decreases from

Table 1 Comparative study of the photocatalytic efficiencies of the different photocatalysts

Catalyst	Conc. of dye (mg L^{-1})	Amount of catalyst (mg)	% Degradation	Degradation time (min)	Light source	Ref.
TiO_2/rGO (5%)	10	120	97.6	120	100 W xenon lamp	55
CdNiZnO	20	30	98.0	50	UV-visible light	56
$Bi_4O_5Br_2$-doped ZSM-5	20	50	99.8	25	300 W Xe lamp	57
CdS/Bi_2S_3/$BiOIO_3$	10	20	94.2	30	300 W Xe lamp	33
$Sr_xBi_{2-x}S_3$	10	5	92.0	240	Visible light	58
Bi_2S_3/g-C_3N_4	10	20	99.9	60	Visible light	59
α/β-CdS/SiO_2	400	50	93.4	60	150 mW cm^{-2}	60
CdS NPs	100	20	99.7	60	300 W xenon lamp	61
FeMCM-41@FePOM	10	5	97.0	40	100 W white LED light	62
10 MCM@BS/CdS	10	50	99.3	60	300 W Xe light	This work

0.044 to 0.011 min^{-1} as the initial concentration increases, while the corresponding half-life ($t_{1/2}$) increases from 15.75 to 63.01 min. The R^2 values indicate good agreement with the pseudo-first-order kinetic model, ranging from 0.843 to 0.981. These results suggest that higher initial dye concentrations slow down the degradation rate, likely due to reduced availability of active sites and light attenuation at higher concentrations.

Moreover, evaluating the reusability of the 10MCM@BS/CdS photocatalyst is crucial to understanding its long-term stability. The reusability test was performed for five photocatalytic cycles. After each cycle, the photocatalyst was recovered by centrifugation, followed by drying and reweighing before reuse. Only a negligible loss of catalyst was observed, resulting in a minor decrease in photocatalytic activity. As shown in Fig. 7a, RhB degradation maintained a consistent efficiency of approximately 94% using the 10MCM@BS/CdS catalyst over the consecutive cycles. The findings demonstrate the catalyst's strong reusability, with the minor reduction in photocatalytic performance likely due to a small amount of catalyst lost during recovery and recycling.

To investigate the reactive species responsible for RhB photodegradation, radical scavenging experiments were conducted using different scavengers. Disodium ethylenediaminetetraacetate (EDTA-2Na), benzoquinone (BQ), and isopropanol (IPA) were employed as quenchers of photogenerated holes (h^+), superoxide radical anions ($^{\bullet}O_2^-$), and hydroxyl radicals ($^{\bullet}OH$), respectively. These quenching agents were introduced into the photocatalytic system during the degradation reaction using the 10MCM@BS/CdS composite. As shown in Fig. 7b, complete degradation (~99.3%) was achieved in the absence of any scavenger. Upon the addition of the three scavengers, a remarkable decrease in the degradation of the dye was observed, indicating the crucial role of the h^+, $^{\bullet}O_2^-$, and $^{\bullet}OH$ radicals in the degradation process. Upon the addition of EDTA-2Na and BQ, the degradation efficiency significantly decreased to 26.7% and 37.8%, respectively, indicating that h^+ and $^{\bullet}O_2^-$ species play dominant roles in the degradation process. In contrast, the presence of IPA resulted in a relatively smaller decrease in degradation efficiency (81.8%), suggesting that $^{\bullet}OH$ radicals play a minor role in the photocatalytic reaction.

The 10MCM@BS/CdS nanocomposite shows impressive photocatalytic performance under visible light, thanks to the combined effect of its heterojunction structure and mesoporous support (Fig. 7c). Under the light source illumination, electron–hole (e^-/h^+) pairs were produced from the photoexcitation of

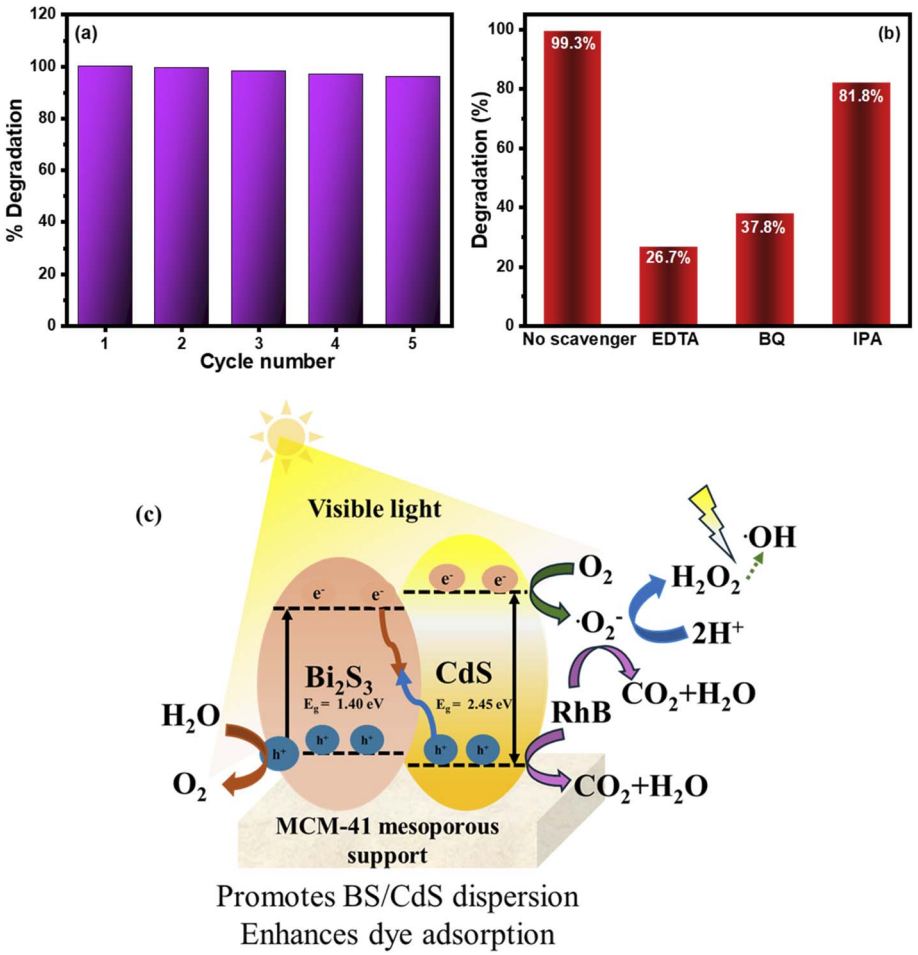

Fig. 7 (a) Photodegradation recycling, (b) effect of scavengers on the RhB photocatalytic degradation using 10MCM@BS/CdS, and (c) diagram illustrating photocatalytic degradation of 10MCM@BS/CdS.

both BS (bandgap ≈ 1.4 eV) and CdS (bandgap ≈ 2.45 eV). As illustrated in eqn (5)–(13), the induced electron–hole (e^-/h^+) pairs interact with dissolved oxygen species (ROS), producing different superoxide radicals. The accumulated electrons in the CB of CdS react with dissolved oxygen (O_2) to produce superoxide radicals ($^{\bullet}O_2^-$), which play a significant role in the degradation process. Meanwhile, the holes in the VB of CdS directly participate in the oxidation of RhB molecules. Due to the relatively less positive VB potential of CdS and the experimental scavenger results, the formation of hydroxyl radicals ($^{\bullet}OH$) is considered limited and plays a minor role in the degradation pathway. Notably, $^{\bullet}OH$ radicals can be generated indirectly *via* secondary reactions involving superoxide radicals, where the stepwise reduction of O_2 leads to the formation of hydrogen peroxide (H_2O_2), which can subsequently decompose to yield $^{\bullet}OH$ radicals under suitable conditions.[23] Furthermore, MCM-41 primarily acts as a high-surface-area mesoporous support that enhances the dispersion of active components and improves dye adsorption near reactive sites. This structural advantage facilitates charge transfer and reduces recombination probability indirectly.

1- Photoexcitation:

$$BS + h\nu \rightarrow BS\ (h_{VB}^{+} + e_{CB}^{-}) \quad (5)$$

$$CdS + h\nu \rightarrow CdS\ (h_{VB}^{+} + e_{CB}^{-}) \quad (6)$$

2- Z-scheme charge transfer:

$$h^+\ (VB, CdS) + e^-\ (CB, BS) \rightarrow \text{recombination} \quad (7)$$

3- Water oxidation

$$2H_2O + h_{VB}^{+} \rightarrow O_2 + 4H^+ \quad (8)$$

4- Superoxide formation:

$$e^-\ (CB, CdS) + O_2 \rightarrow {}^{\bullet}O_2^- \quad (9)$$

5- H_2O_2 formation (stepwise reduction)

$$^{\bullet}O_2^- + H^+ \rightarrow HO_2^{\bullet} \quad (10)$$

$$2HO_2^{\bullet} \rightarrow H_2O_2 + O_2 \quad (11)$$

6- Secondary $^{\bullet}OH$ formation

$$H_2O_2 + e^- \rightarrow OH^- + {}^{\bullet}OH \quad (12)$$

7- Dye degradation

$$RhB + {}^{\bullet}OH/{}^{\bullet}O_2^-/h^+\ (VB, CdS) \rightarrow CO_2 + H_2O \quad (13)$$

4. Conclusion

In conclusion, the MCM-41 doped Bi_2S_3/CdS composites with different MCM contents were prepared through the hydrothermal method. A variety of analytical and spectroscopic techniques were employed to characterize the as-prepared nanocomposites. The combination of MCM-41 with Bi_2S_3/CdS composite can increase the surface area, suppress the agglomeration of Bi_2S_3/CdS nanoparticles, and facilitate charge separation and transport, enhancing the photocatalytic activity. TEM and HR-TEM analysis confirmed the uniform dispersion of Bi_2S_3/CdS heterojunction within MCM-41, facilitating efficient charge transfer. Furthermore, electrochemical investigations supported the key role of combining the Bi_2S_3/CdS heterostructure with the MCM-41 support in enhancing the photoelectrochemical properties. Among all composites, the 10MCM@BS/CdS sample exhibited a stable photocurrent density of ~85 μA cm^{-2} through *I–t* measurements. Mott–Schottky analysis indicated n-type semiconductor behaviour with an increased charge carrier density and more negative flat-band potential (~−0.59 V *vs.* Ag/AgCl). Besides, EIS results showed the smallest Nyquist semicircle, confirming the lowest charge-transfer resistance (55 Ω) and suppressed electron–hole recombination. Accordingly, the as-prepared catalyst showed superior visible-light photocatalytic activity, reaching 99.3% RhB degradation within 60 min, obeying pseudo-first-order kinetics with excellent stability over repeated cycles. Overall, the synergistic heterojunction–mesoporous design enhances the photocatalytic and electrochemical performance for solar-driven wastewater treatment.

Conflicts of interest

The authors declare no competing financial interest.

Data availability

All data underlying the results are available as part of the article and no additional source data is required.

References

1 A. du Plessis, *One Earth*, 2022, **5**, 129–131.
2 A. Nader, D. A. Kospa, A. I. Ahmed, A. Awad Ibrahim and O. A. Elbanna, *Sep. Purif. Technol.*, 2025, **354**, 128776.
3 S. Tarannum, M. Sahadat Hossain, M. Saiful Alam, N. Mohammed Bahadur and S. Ahmed, *J. Photochem. Photobiol., A*, 2024, **447**, 115271.
4 A. A. Ibrahim, D. A. Kospa, S. Orabi, S. M. Abo Kamar, A. A. Salah, E. A. El-Sharkawy, S. A. El-Hakam and A. I. Ahmed, *RSC Adv.*, 2025, **15**, 26608–26622.
5 S. Benkhaya, S. M' rabet and A. El Harfi, *Inorg. Chem. Commun.*, 2020, **115**, 107891.
6 M. F. Lanjwani, M. Tuzen, M. Y. Khuhawar and T. A. Saleh, *Inorg. Chem. Commun.*, 2024, **159**, 111613.
7 A. P. Periyasamy, *Cleaner Water*, 2025, **4**, 100092.
8 L. Piai, M. Blokland, A. van der Wal and A. Langenhoff, *J. Hazard. Mater.*, 2020, **388**, 122028.
9 M. Wu, W. Yu, J. Qu and J. Gregory, *Water Res.*, 2019, **155**, 131–141.
10 Y. Zhang, X. Hong, X.-M. Cao, X.-Q. Huang, B. Hu, S.-Y. Ding and H. Lin, *ACS Appl. Mater. Interfaces*, 2021, **13**, 6359–6366.

11 T. Liu, H. Zhou, N. Graham, W. Yu and K. Sun, *Water Res.*, 2019, **156**, 425–433.
12 R. Jiang, G. Lu, Z. Yan, D. Wu, R. Zhou and X. Bao, *Chem. Eng. J.*, 2019, **374**, 79–90.
13 A. Asghar, A. A. Abdul Raman and W. M. A. Wan Daud, *J. Cleaner Prod.*, 2015, **87**, 826–838.
14 H. Alamgholiloo, S. Nazari, E. Asgari, A. Sheikhmohammadi, B. Hashemzadeh, N. Ghasemian, M. Bigdeloo and A. Ehsani, *J. Mol. Liq.*, 2022, **364**, 119990.
15 A. Chakravorty and S. Roy, *Sustainable Chem. Environ.*, 2024, **8**, 100155.
16 A. K. Pandey, R. Reji Kumar, K. B, I. A. Laghari, M. Samykano, R. Kothari, A. M. Abusorrah, K. Sharma and V. V. Tyagi, *J. Environ. Manage.*, 2021, **297**, 113300.
17 X. Li, Y. Chen, Y. Tao, L. Shen, Z. Xu, Z. Bian and H. Li, *Chem Catal.*, 2022, **2**, 1315–1345.
18 H.-Y. Ma, L. Zhao, L.-H. Guo, H. Zhang, F.-J. Chen and W.-C. Yu, *J. Hazard. Mater.*, 2019, **369**, 719–726.
19 H. Tong, S. Ouyang, Y. Bi, N. Umezawa, M. Oshikiri and J. Ye, *Adv. Mater.*, 2012, **24**, 229–251.
20 M. Farrag, *Sci. Rep.*, 2023, **13**, 17634.
21 M. E. Rincón, H. Hu, x Martı, G. nez, R. Suárez and J. G. Bañuelos, *Sol. Energy Mater. Sol. Cells*, 2003, **77**, 239–254.
22 M. Sahu and C. Park, *Mater. Today Sustainability*, 2023, **23**, 100441.
23 S. M. Ghoreishian, K. S. Ranjith, B. Park, S.-K. Hwang, R. Hosseini, R. Behjatmanesh-Ardakani, S. M. Pourmortazavi, H. U. Lee, B. Son, S. Mirsadeghi, Y.-K. Han and Y. S. Huh, *Chem. Eng. J.*, 2021, **419**, 129530.
24 L. Ding, C. Geng, Y. Hao, K. Ma, M. Liu, P. He, Z. Chen and Q. Chen, *Inorg. Chem. Commun.*, 2025, **178**, 114542.
25 L. Jie, X. Gao, X. Cao, S. Wu, X. Long, Q. Ma and J. Su, *Mater. Sci. Semicond. Process.*, 2024, **176**, 108288.
26 J. Wang, C. Liu, Y. Wang, P. Shen, Y. Mu, F. Jia, T. Zhou, F. Xing, G. Yin and M. Sun, *SN Appl. Sci.*, 2020, **2**, 2009.
27 S. Sambyal, A. Sudhaik, S. Sonu, P. Raizada, V. Chaudhary, V.-H. Nguyen, A. A. P. Khan, C. M. Hussain and P. Singh, *Coord. Chem. Rev.*, 2025, **535**, 216653.
28 J. Xin, P. Dong, L. Pu, H. Tan and J. Li, *Colloids Surf., A*, 2014, **450**, 25–35.
29 Y. Zhang, Q. Chen, Q. Xiao, L. Shi, Z. Zhao and H. Wang, *Chemosphere*, 2023, **335**, 139022.
30 W. Wang, J. Xue and J. Liu, *J. Mater. Chem. A*, 2024, **12**, 10659–10675.
31 A. Nazir, M. S. Tahir, G. M. Kamal, X. Zhang, M. B. Tahir, B. Jiang and M. Safdar, *Molecules*, 2023, **28**, 3167.
32 M. Li, H. Yao, S. Yao, G. Chen and J. Sun, *J. Colloid Interface Sci.*, 2023, **630**, 224–234.
33 M. Dai, R. Xue, M. Liu and Z. Wang, *J. Alloys Compd.*, 2024, **971**, 172784.
34 I. Velo-Gala, J. J. López-Peñalver, M. Sánchez-Polo and J. Rivera-Utrilla, *Appl. Catal., B*, 2013, **142–143**, 694–704.
35 V. Blanchard, Z. Asbai, K. Cottet, G. Boissonnat, M. Port and Z. Amara, *Org. Process Res. Dev.*, 2020, **24**, 822–826.
36 K. Mojsilović, N. Božović, S. Stojanović, L. Damjanović-Vasilić, M. Serdechnova, C. Blawert, M. L. Zheludkevich, S. Stojadinović and R. Vasilić, *Surf. Interfaces*, 2021, **26**, 101307.
37 A. Y. Shan, T. I. M. Ghazi and S. A. Rashid, *Appl. Catal., A*, 2010, **389**, 1–8.
38 V. Candela-Noguera, M. Alfonso, P. Amorós, E. Aznar, M. D. Marcos and R. Martínez-Máñez, *Microporous Mesoporous Mater.*, 2024, **363**, 112840.
39 A. A. Ibrahim, D. A. Kospa, O. R. Hayes, A. S. Khder, S. A. El-Hakam and A. I. Ahmed, *RSC Adv.*, 2023, **13**, 15243–15260.
40 A. E. R. S. Khder, H. M. A. Hassan and M. S. El-Shall, *Appl. Catal., A*, 2012, **411–412**, 77–86.
41 X. Li, J. Chen, H. Li, J. Li, Y. Xu, Y. Liu and J. Zhou, *J. Nat. Gas Chem.*, 2011, **20**, 413–417.
42 J. Chao, H. Li and S. Xing, *Solid State Sci.*, 2019, **98**, 106034.
43 F. Yang, X. Tian, K. Zhang, X. Zhang and L. Liu, *ECS J. Solid State Sci. Technol.*, 2018, **7**, P311–P316.
44 Y. P. Bernal, J. Alvarado, R. L. Juárez, M. Á. Méndez Rojas, E. A. de Vasconcelos, W. M. de Azevedo, S. A. Iniesta and J. V. Cab, *Optik*, 2019, **185**, 429–440.
45 J. Xu, Y. Ao and M. Chen, *Mater. Lett.*, 2013, **92**, 126–128.
46 X. Geng, D. Zhang, Z. Zheng, G. Ye, S. Li, H. Tu, Y. Wan and P. Yang, *Nano Energy*, 2021, **82**, 105700.
47 J. Liu, S. Liu, Y. Li, J. Xue, Y. He, F. Liu, L. Yang, J. Hu, Z. Xiong and L. Long, *RSC Adv.*, 2019, **9**, 40835–40844.
48 P. K. Bankar, M. S. Pawar, A. S. Pawbake, S. S. Warule, D. J. Late and M. A. More, *RSC Adv.*, 2016, **6**, 95092–95100.
49 Y. Olivares, C. Herrera, J. Seguel, C. Sepúlveda, C. Parra and G. Pecchi, *Catalysts*, 2023, **13**, 1024.
50 W. Guo, A. B. Posadas and A. A. Demkov, *J. Appl. Phys.*, 2020, **127**, 055302.
51 D. Li, P. Yan, Q. Zhao, X. Bai, X. Ma, J. Xue, Y. Zhang and M. Liu, *J. Inorg. Organomet. Polym.*, 2020, **30**, 5100–5107.
52 R. K. Chava, Y. Im and M. Kang, *J. Mater. Chem. A*, 2024, **12**, 18498–18511.
53 Z. Yan, L. Du and D. Lee Phillips, *RSC Adv.*, 2017, **7**, 55993–55999.
54 Y. Xiong, D. Zhang, X. Zhao, B. Peng, P. Yu and Z. Cheng, *ChemSusChem*, 2024, e202400515, DOI: 10.1002/cssc.202400515.
55 S. H. Alwan, K. H. Salem and H. A. Alshamsi, *Mater. Today Commun.*, 2022, **33**, 104558.
56 S. Khan, D.-S. Kim, M. Ullah, M. Sadiq, N. Muhammad, M. Khan, A. Noor and S. Qayyum, *Sci. Rep.*, 2025, **15**, 31947.
57 M. Zhang, X. Sun, C. Wang, Y. Wang, Z. Tan, J. Li and B. Xi, *Mater. Chem. Phys.*, 2022, **278**, 125697.
58 A. Sharma, A. Makhija, L. Saini, A. Ohlan, S. Dahiya, R. Punia and A. S. Maan, *J. Taiwan Inst. Chem. Eng.*, 2024, **161**, 105534.
59 K. Yang, Y. Yang, Y. Jiang, B. Ye, L. Li, W. Liu, T. Yan, W. Li and S. Liu, *Surf. Interfaces*, 2024, **52**, 104885.
60 W. Wang, X. Qin, X. Wang, K. Ma, Z. Wu, H. Si and J. Zhang, *Environ. Pollut.*, 2024, **345**, 123428.
61 X. Qin, W. Wang, K. Liu, Q. Li and J. Zhang, *Appl. Surf. Sci.*, 2023, **609**, 155320.
62 R. Hajian and F. D. Rahmatabadi, *Mater. Res. Bull.*, 2025, **188**, 113368.